Smart Materials & Structures, 21:1–11, 2012.

Dynamic Roughness and Power Dissipation of Polymer Films Actuated with Liquid Crystal Polymer Inclusions

E. J. Barbero[1], D. R. Cairns, and V. H. Mucino
Mechanical and Aerospace Engineering, West Virginia University,
Morgantown, WV 26506-6106, USA
and
J. A. Mayugo
Mechanical Engineering and Industrial Construction, Universitat de Girona,
Girona, 17071, Spain

1 Abstract

Analytical and numerical tools for the analysis and design of actuated polymer films (APF) are developed and described in this manuscript. Computational micromechanical models are set up and correlated in order to calculate the deformation and power requirement to actuate the APF taking into account hyperelastic and viscous effects. A method is developed to correlate material parameters in the viscous branch of the Bergström-Boyce model to available experimental data. The effect of various geometric and material parameters are elucidated by a parametric study including coherent vs. non-coherent actuators, excitation frequency and magnitude, modulus of elasticity of the actuator and the top film, and actuator volume fraction.

2 Keywords

Dissipation, Actuated Polymer Films, Finite Element, Hyperelasticity, Viscoelasticity, Bergström-Boyce

3 Introduction

Actuated polymer films (APF) are a novel kind of material that can be actively actuated with an external stimulus in order to excite a physical response without requiring any type of mechanical mechanisms.

The idea of dispersing liquid crystals in a polymer and actuate them by means of an electric field is not new, but most of the research efforts have been oriented towards switchable electro-optical properties [1–7] and holographic materials [8, 9]. Some of the sought applications described

[1]Corresponding author. The final publication is available at http://dx.doi.org/10.1088/0964-1726/21/1/015003

in the aforementioned references include electrically switchable windows, liquid crystal displays, and optically switching gratings, while the present work focus on the change of shape of the film, specifically inducing roughness on the surface of the film.

Several authors [1–7] have made important contributions regarding development and application of liquid crystal (LC) polymers as optoelectronic materials. Doane [1] and Drzaic [2] report LC polymers having unique properties which are expected to expand LC technology into new display and light shutter applications. Tanaka [3] presents layered polymer dispersed liquid crystals (PDLC) capable of reflecting and transmitting light a specific wavelengths. Mucha [4] does an extensive review on the different preparation methods and applications of liquid crystals, polymer blends, and composites. Crawford [5] presents a way to capture different patterns in the nematic order of the dispersed liquid crystals. Bunning [6] reviews the development of holographic polymer dispersed liquid crystals (H-PDLCs), where a coherent laser is used to create the grating. A detailed review of computer simulation models, both for LC and PDLC, is presented by Jeon [7]. However, with the exception of [10], PDLCs have not been used as electrostatic actuators to effect surface deformations on the film, thus providing the motivation for this study.

In the context of this work, the actuator polymer films considered are made of electrically responsive LC polymer ellipsoids embedded in a polymeric film. When the LC actuators are subjected to an electric field, they try to align with the field gradient [10]. Therefore, upon application of the electric field, the actuators will deform the surrounding polymeric material as they align with the electric field. Since the size of the actuators is of the same order of magnitude of the film thickness, changes in the morphology of the film surface take place, enabling to dynamically control its roughness by means of the applied electric field. There are applications where switching the roughness between on and off is desired, while in other cases the roughness has to change periodically. In the former case, the switching time is one of the most important parameters while in the latter, the power required to actuate the APF is a key parameter.

The goal of the present work is to develop computational tools to study dynamic switchable surface roughness. While static roughness can be analyzed also, it is not the primary concern of this work.

Potential applications include tactile responsive touch panels, dust mitigation systems for solar panels and other devices, and tunable hydrophobicity surfaces. Another possible application of these novel materials is in the aerodynamic flow control field. Flow separation in airfoils can be reduced when the leading edge can change its roughness at specific frequencies and amplitudes (sub-boundary layer) [11–13]. Reductions in the flow separation can result in lift enhancement, drag reduction or both. A crucial factor in the feasibility of the application of dynamic roughness for flow control is that the power savings associated with the improved aerodynamics must be greater that the power required to actuate the APF. Therefore, the ability to calculate the power consumption and the roughness achieved when the APF is actuated is of paramount importance.

Although power consumption and roughness could be determined with physical testing, it would be too costly and time consuming. Since the actuated polymer film technology is new and still under development, numerical modeling allows us to explore different scenarios in advance. For example, currently, the liquid crystal actuators are embedded in polyvinyl alcohol (PVA) [10], but because PVA is soluble in water, it could not be used for dynamic roughness applications in aircraft wings. Therefore, different materials (possibly rubbery elastomers) should be analyzed as possible candidates. Furthermore, many achievable geometric configurations (varying the actuator's geometry, film thickness, etc.) can be explored by modeling.

The key component in the actuated polymer films are the actuators themselves. Responsive liquid crystal rods have been developed by Cairns et al. [14, 15]. The first potential applications sought for these actuators were active mixing in microfluidic channels and electro-rheological fluids

[14]. More recently, the idea of embedding these actuators in a polymeric film was investigated by Morris et al. [10]. Currently the electric field is applied to the film when it is placed between two plates of indium-tin oxide (ITO) coated glass. For applications like aerodynamic flow control, at least one of the plates must be removed and the external surface of the APF should be coated with an electrically conductive thin layer in order to apply the voltage differential.

Since the possible applications of the actuated polymer films require a measurable change in the roughness of the surface, the deformations are expected to be finite. Therefore a hyperelastic model should be used. The Arruda and Boyce [16] model is used in this study, but other models can be easily substituted.

Since some applications of APF require cyclic excitation at low power consumption, the viscous effects must be modeled [17]. Furthermore, since strains are expected to be large, nonlinear stress-strain effects must be included in the model. Finally, since the excitation frequency is expected to be variable, rate dependency effects must be included.

A relatively new constitutive model for large strain, time-dependent, elastomeric materials has been developed by Bergström and Boyce [18,19]. This model has the ability to capture the viscous rate-dependence and the non-linear relationship between stress and strain. This model was later slightly modified to improve the hysteretic behavior of the model under cyclic loading [20]. The Bergström-Boyce (BB) model has been also successfully used to model soft biological tissues [20] and filled elastomers [21,22].

In the recent years, some authors have worked on the finite element implementation of the BB model [23–25]. Furthermore, the BB model has been implemented in general purpose commercial finite element packages like ABAQUS® and ANSYS®. Temperature dependent properties and aging [26] have not been considered in this work but could be implemented in the future.

This work presents a novel methodology to calculate the dissipated energy of an elastomer actuated dynamically by a periodic electrostatic field that effects the embedded LC inclusions. Also, this work presents a methodology to simulate the macro-mechanical behavior of a Polymer Dispersed Liquid Crystal (PDLC), that is, of an elastomer film actuated by LC polymer inclusions. Furthermore, this work is novel in that develops an useful design tool that predicts the 3D response of the system in terms of a more practical, computationally efficient 2D model.

4 Modeling Aspects

Procedures for the calculation of the power required to actuate the APF and the roughness obtained on the surface of the film comprise the core of the present work.

In Sections 5 and 6, diluted[2] two- and three-dimensional models are developed, respectively. These models have only one actuator embedded in the base film, which is modeled with a width of five times the actuator's length. This is purposely done to analyze the case where the actuators are far from each other (diluted case). The results from these models are used in Section 7 to correlate the roughness and dissipation between the two- and three-dimensional models, as a function of the volume fraction V_f. In this way, the two-dimensional model can be used for design once correlated to more accurate predictions obtained by the three-dimensional model.

Lastly, in Section 8, a series of parametric analysis are performed using the two-dimensional model. Specifically, the top surface response (roughness) and dissipation power are analyzed varying the geometry and frequency of excitation.

[2]In a diluted model, the separation between the actuators is large enough to consider that the interaction among actuators is negligible.

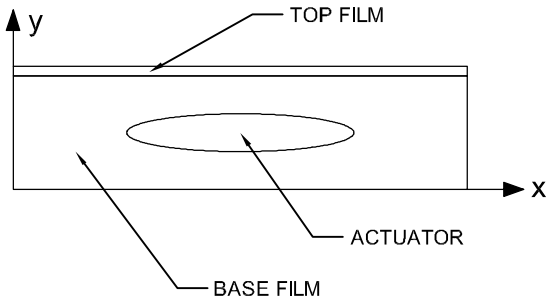

Figure 1: Geometry of the 2D representative volume element.

A representative volume element (RVE, [27, §4.1.2]) for the APF is shown in Figure 1. The width of the RVE is along the x direction, the thickness is along the y direction and that the depth runs along the z direction.

In the development of the finite element models, three materials are defined. One for the actuator (ellipse in two-dimensional models and ellipsoid in three-dimensional models), other for the base film where the actuator is embedded and lastly, one for the top film. The top film must be electrically conductive, in order to apply the voltage potential to actuate the ellipses/ellipsoids[3]. The electrostatic pressure developed between the electrodes is neglected. Moreover, perfect adhesion between the actuators and the polymer where they are casted is considered.

The actuator is modeled using a linear elastic material model, with Young's modulus $E = 3000\,\text{MPa}$ and Poisson ratio $\nu = 0.3$. A parametric study of the effect of changing the actuator Young's modulus is presented in Section 8.

The dissipative response of the base film is modeled using the BB model [19, 21]. The elastic response follows the hyperelastic model proposed by Arruda and Boyce [16] with material parameters fit to DuPont's Hytrel 4056 (TPE) elastomer. The equilibrium (relaxed) properties were obtained from CAMPUS Database [28].

The base film material is assumed to be incompressible, a reasonable hypothesis for most elastomers. Under the assumption of incompressibility many simplifications can be done in the kinematic equations but some special considerations must be taken when applying the finite element method in Sections 5, 6 and 8.

The parameters of the Arruda-Boyce hyperelastic model are: the shear modulus of the hyperelastic network μ_A, the limiting chain stretch λ_A^{lock} and the compressibility parameter d. The models developed in forthcoming sections are illustrated with properties fitted to stress-strain data for Hytrel 4056. The hyper-elastic portion of the model parameters can be obtained with the material fitting procedure available in ABAQUS® , yielding $\mu_A = 4.68\,\text{MPa}, \lambda_A^{\text{lock}} = 5311.53$ and $d = 0.00/\text{MPa}$ (incompressible).

There are four remaining parameters of the BB Model that characterize the time dependent, hysteretic behavior of the material. These are: the stress scaling factor s, the creep parameter $\dot{\gamma}_0/\tau_{\text{base}}^m$, the effective stress exponent m, and the creep strain exponent c. The procedure described in Section 9 is used to obtain the values for these parameters from experimental data. Lacking data for Hytrel 4056 that would display its hysteretic behavior, the values were obtained from data for nitrile rubber: $s = 2.0, \dot{\gamma}_0/\tau_{\text{base}}^m = 0.5/(s\ \text{MPa}^m), m = 4.5$ and $c = -1.0$.

[3]The words ellipsoid and ellipse will used interchangeably, although strictly speaking ellipsoid should be used only for three-dimensional geometries while ellipse for two-dimensional geometries.

The top film is modeled using a linear elastic material model, with assumed Young's modulus $E = 70\,000$ MPa and Poisson ratio $\nu = 0.3$. A parametric study of the effect of changing the top film modulus is presented in Section 8.

All the models developed in this manuscript represent a portion of the whole structure. It is assumed that this portion or substructure repeats itself periodically. If the geometry, material properties, boundary conditions and load are periodic, the solution has to be periodic too. When modeling the substructure it is necessary to recover this periodic behavior on the boundaries of the model. This is achieved using periodic boundary conditions [29, §2.3.4 and §6.2].

The top and bottom surfaces of each ellipse are loaded, respectively, in opposite directions with a uniform distributed load applied in the x direction (parallel to the ellipse major axis) to generate the torque. It is assumed that the magnitude of the the load does not change if the surfaces change their size during the deformation. It could be argued that the magnitude of the load should change when the actuator rotates with respect to the electric field, but the rotations are so small that $\cos\alpha = 0.9998$, where α is the maximum rotation angle. The angle was calculated from the model "3D-2" listed in Table 2. Also, it is assumed that the direction does not change when the the ellipses deforms (no following forces).

The magnitude of the distributed traction that generates the torque is assumed to be 10 MPa. This value was adopted because the resultant displacements from the models are in good agreement (same order of magnitude) with experimental results done in an alike actuated polymer film [10]. In Section 8, magnitudes of 5 MPa and 15 MPa will be also considered to reveal their effect on the response.

Furthermore, it is assumed that the actuators generate torque by a volume and not by an area effect. Cairns et al. propose an equation where the generated torque due to the applied electric field is proportional to the volume V of the actuator, both for cylindrical [14, Equation 1] and spherical [30, Equation 1] geometries. In the latter reference, the torque per unit volume Γ is explicitly defined.

The uniform distributed load has a sinusoidal function of time,

$$F_x(t) = A\ \sin(B\ t) \tag{1}$$

where A is the amplitude and $2\pi B$ is the period of the excitation.

The solver is set to a time increment size equal or smaller than 1/120 of the excitation period. The duration of the analysis matches the excitation period. Therefore, at least 120 steps are used to solve the problem. Such a fine time discretization is done because the results from each time step will be used to integrate the dissipation energy during the post-processing.

Although ABAQUS® has the option to calculate the creep dissipated energy in the model (History Output `ALLCD`), the results are not accurate. For one particular example, it was found that the dissipated energy calculated by ABAQUS® was over twice than expected. Therefore, a PYTHON script is used to do this calculation. This script is described in A.

In this work, the dissipated energy at one point is defined as the difference between the recoverable elastic energy and the integral between the stress-strain curve. Inertial forces, and therefore kinetic energy, are neglected. For the whole model, the problem reduces to do this integration at each integration point and then to integrate over the volume of model. If the resulting dissipation energy is divided by the duration of the analysis, then a dissipation power can be calculated. Lastly, for application purposes, it is useful to divide the dissipation power by the area (width times depth) of the RVE, which defines the surface dissipation power.

The roughness is defined as the difference between the maximum and minimum vertical displacement of the top surface of the RVE. For time dependent loadings, a difference can be calculated for

Component	Width [µm]	Thickness [µm]	Depth [µm]
Ellipse	60	10	∞
Base Film	300	30	∞
Top Film	300	0.03	∞

Table 1: Dimensions of the 2D representative volume element.

each time frame in the solution process. In this case, the roughness will be the maximum of these differences over all the time frames.

5 Two-dimensional Model

The objective of the two-dimensional model is to analyze the case where the actuators are sufficiently apart from each other that they don't interact (diluted case). The results from this model and the model developed in Section 6 will be used later in Section 7 to correlate the results of two-dimensional and three-dimensional models as a function of the volume fraction V_f.

Plane strain is assumed for this model. The RVE includes the base film with one embedded actuator and an electrically conductive film on the top surface of the device. A schematic representation of the RVE is shown in Figure 1 with dimensions shown in Table 1.

For some of the applications, the required excitation frequency is expected to be in the 30 Hz to 200 Hz range. In this section, the frequency of the load applied by the actuator is 200 Hz. A parametric analysis varying the magnitude and frequency of the excitation is presented in Section 8.

The geometry is discretized predominantly with linear, quadrilateral, continuum plane strain elements. The base film is discretized with reduced integration, hybrid elements (`CP4RH`). Hybrid elements must be used when simulating incompressible materials. ABAQUS® Theory Manual [31, §3.2.4] also suggests that reduced integration elements should be used when modeling incompressible materials at finite strain. The actuator is discretized using reduced integration (`CP4R`) elements, because it is an cost-effective method if the solution is expected to be smooth or if the stresses and/or strains in the region are not of concern. Only a few (314 out of 13621) constant strain triangular elements are used to improve mesh transitions. The triangular elements used are `CPE3` and `CPE3H`, the former in the actuator and the latter in the base film.

The calculated dissipation power per unit surface and roughness for this analysis are shown in Table 2, Model 2D-1.

6 Three-dimensional Model

The objective of the three-dimensional model is to analyze the actuated polymer film considering its geometry in full three-dimensional detail. The results of the three-dimensional models developed in this section will be correlated with the results obtained in the previous section for the two-dimensional, diluted model. The correlation between these results is presented in Section 7.

Symmetry is exploited in all three-dimensional models. In Figure 2, the 3D RVE is split along the length of the ellipsoid to exploit symmetry. Then, only one half of the RVE is discretized to reduce the computational time. The dimensions of the RVE are given in Table 3.

[1]Since this result is from a plane strain model, the units are per mm depth. Thus, they should not be compared with the other results under this column.

Model	Volume Fraction	RVE Depth	Dissipation Power	Surf. Dissip. Power	Roughness	Elements
	[%]	[µm]	[nW]	[µW/mm^2]	[µm]	[ ]
2D-1	5.23	∞	12638.0[1]	42.1	0.9440	13621
3D-1	3.32	5.25	49.6	31.4	0.8344	12482
3D-2	1.92	9.1	31.0	11.4	0.5146	16630
3D-3	1.39	12.5	29.4	7.8	0.4512	25970
3D-4	0.70	25	26.4	3.5	0.4487	33976

Table 2: Results for the two- and three-dimensional models.

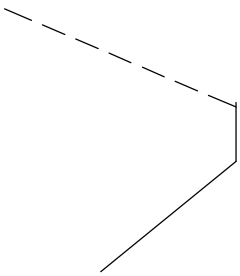

Figure 2: Geometry of the 3D representative volume element.

Component	Width [µm]	Thickness [µm]	Depth [µm]
Ellipsoid	60	10	5
Base Film	300	30	Variable: 5.25 - 25
Top Film	300	0.03	Variable: 5.25 - 25

Table 3: Dimensions of the 3D representative volume element.

Four different volume fractions (0.70 %, 1.39 %, 1.92 % and 3.32 %) are analyzed by changing the depth[4] of the RVE (5.25 µm, 9.81 µm, 12.50 µm and 25.00 µm). With the current manufacturing process used to fabricate the actuated polymer films, there is a minimum theoretical separation between actuators in the direction of the depth of the RVE, given by

$$\min \mathrm{DEPTH} = a\sqrt[3]{\mathrm{AR}} \tag{2}$$

where c, a are the major and minor radii of the actuator, respectively. $\mathrm{AR} = \frac{c}{a}$ is the aspect ratio. In this study, $a = 5\,\mu\mathrm{m}$ and $\mathrm{AR} = 6$. Therefore, the minimum theoretical depth is 9.1 µm. Three of the four cases span between the minimum depth and the equivalent to a separation of 5 minor diameters between the ellipsoids centers. The fourth case (DEPTH = 5.25 µm) is included to have a solution close to what it would be the plane strain condition, as it was assumed in Section 5.

For the three-dimensional models, only one excitation frequency is analyzed. The load applied on the actuator has, as in Section 5, a frequency of 200 Hz. A parametric analysis varying the excitation magnitude and frequency is done in a two-dimensional model in Section 8. The results from the two-dimensional model can be correlated with the three-dimensional case using the ratios defined in Section 7.

The base film is modeled as bonded to the substrate where the APF is applied. Therefore, the three translational degrees of freedom are set to zero on the bottom surface of the base film. The two side surfaces (the surfaces that have the x axis a normal, have periodic boundary conditions enforced between them. Lastly, the front and back surfaces (z axis as normal), have symmetry boundary conditions (UZ=ROTX=ROTY=0).

The mesh is composed of linear, hexahedral, continuum elements. The number of elements varies for each volume fraction V_f analyzed (See Table 2). All the elements of the mesh use a reduced integration scheme. To avoid shear locking, the top film is modeled using `C3D8R` elements. The base film is meshed with reduced integration, hybrid elements (`C3D8RH`).

The RVE is partitioned into twelve cells to allow for structured meshing. Along the width of the RVE, the element size tapers towards the sides of the RVE, where the actuator's effect is negligible. The elements of the top film have a very high aspect ratio, something that is not desirable, but they do not raise an error flag during the analysis because the thickness of the top film is extremely small compared to the two other dimensions. Better shaped elements could be obtained by making a finer mesh, which should have a transition within the base film, but significantly increasing the computational cost of the analysis.

The computational effort to solve the three-dimensional models is considerable. For example, the largest model took 3 h 10 min to solve and post-process in a PC system with a 4-core CPU and 4 GB RAM. The dissipation power, dissipation power per unit surface, and roughness for these analysis are included in Table 2. As the depth of the RVE is increased, the dissipation power per unit area decreases, not only because the neighboring effect is reduced but mostly because the dissipation caused by the actuator is divided by a larger area. In the limit, the surface dissipation tends to zero when the volume fraction goes to zero.

It can be seen in Figure 3 that as the volume fraction V_f decreases, the roughness reaches a limit value corresponding to the roughness of a single actuator. Since the surface dissipation power is defined as dissipation per unit area of film, its value tends to zero as the volume fraction tends to zero; i.e., if a single actuator, which has a finite dissipation power, is embedded in a infinite medium, the dissipation power per unit surface approaches zero.

[4]The depth is in the direction z, normal to the $x - y$ plane in Figure 1

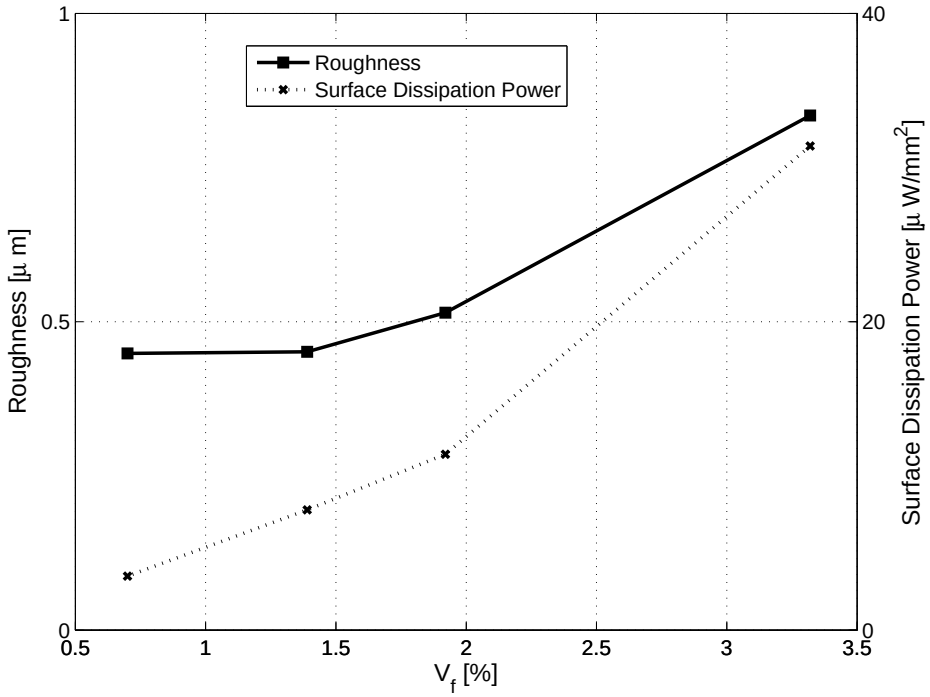

Figure 3: Roughness and Surface Dissipation Power as a function of V_f for the 3D model

7 Correlation between 2D and 3D

Based on the results from Sections 5 and 6, a correlation between the two- and three-dimensional response based on the volume fraction V_f is proposed. For the two-dimensional model the volume fraction V_f is equal to the area fraction A_f, because the model is assumed to be in plane strain. The surface dissipation power and roughness from the two-dimensional model are set as the reference values and the ratios of three-dimensional to two-dimensional results are calculated as a function of the volume fraction, as follows:

$$r_{[\bullet]}\left(V_f\right) = \frac{[\bullet]_{3\mathrm{D}}\left(V_f\right)}{[\bullet]_{2\mathrm{D}}\left(A_f\right)} \tag{3}$$

The calculated ratios r_R, r_D for the roughness and dissipation, respectively, are shown in Figure 4.

These results were calculated for a sinusoidal load with 10 MPa amplitude and 200 Hz frequency for an RVE width of 300 µm, resulting in $A_f = V_f = 5.23\,\%$ for the two-dimensional case.

As it can be seen in Figure 4, the roughness ratio has a plateau for volume fractions smaller than 1.5 %. This means that the roughness of the APF as predicted by a full 3D analysis is no less than 50% of the 2D prediction, making the later into a useful design tool. Further, using (3), the results of a 3D analysis can be predicted from the results of a less costly 2D analysis.

8 Parametric Study

In this section a two-dimensional parametric study is done on a RVE with one actuator. Because periodic boundary conditions are enforced, it is assumed that all the actuators are coherent (i.e. all the right tips will go up and all the left tips will go down). Comparison between coherent and not

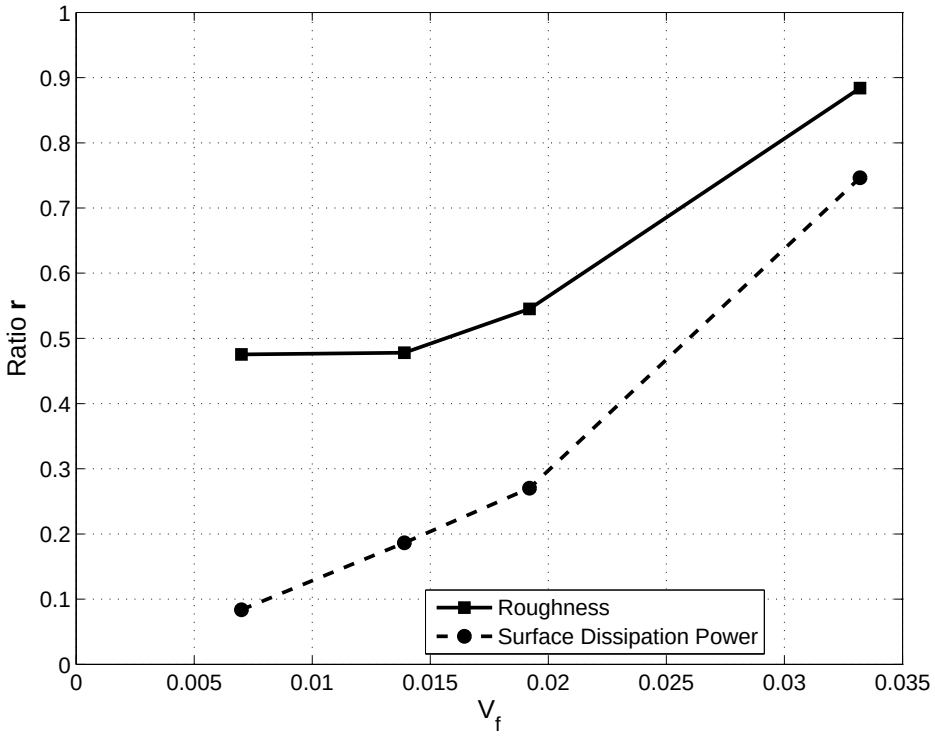

Figure 4: Ratios for roughness and surface dissipation power

coherent actuator response is shown in Figure 5. It can be seen that the roughness amplitudes are similar but the surface profiles are different.

The parameters that will be analyzed are: frequency and magnitude of the excitation, volume fraction (changing the width of the film) and the Young's modulus of the top film and the actuator. Also a mesh dependency analysis is performed to show that the results are convergent.

The results of this section are listed in Table 4. The model 2D-P-01 is set as a reference for comparison purposes in the parametric analyses.

A fixed width (120 µm) of the RVE is considered. The frequency of the excitation is varied from 20 Hz to 200 Hz in increments of 30 Hz. The results are shown in Figure 6, based on models 2D-P-01 to 2D-P-07. While the roughness decreases with increasing excitation frequencies, the surface dissipation power follows the opposite trend (Figure 6). This behavior arises from the viscous network of the base film material model. For a creeping material, it is expected that the strains will grow with time if the load is kept constant. In the case of the actuated polymer films, the higher the frequency, the less time that the base film will have to deform. Thus, the roughness is reduced at higher frequencies.

Regarding the surface dissipation power, higher frequencies of excitation will cause more displacement reversal cycles in the base film. From basic mechanics, it is known that the dissipation in a dash-pot or damper is associated to the first derivative of the displacement with respect to time, which for a sinusoidal movement becomes maximum when the displacement is reversed from positive to negative or vice versa.

As the torque generated by actuators depends on the intensity of the electric field applied, and the magnitude of the torque has not been experimentally determined yet, a parametric study is done to assess torque influence on the APF response. In the present work, the torque generated by the actuators is materialized by the application of surface traction on the ellipsoid with the

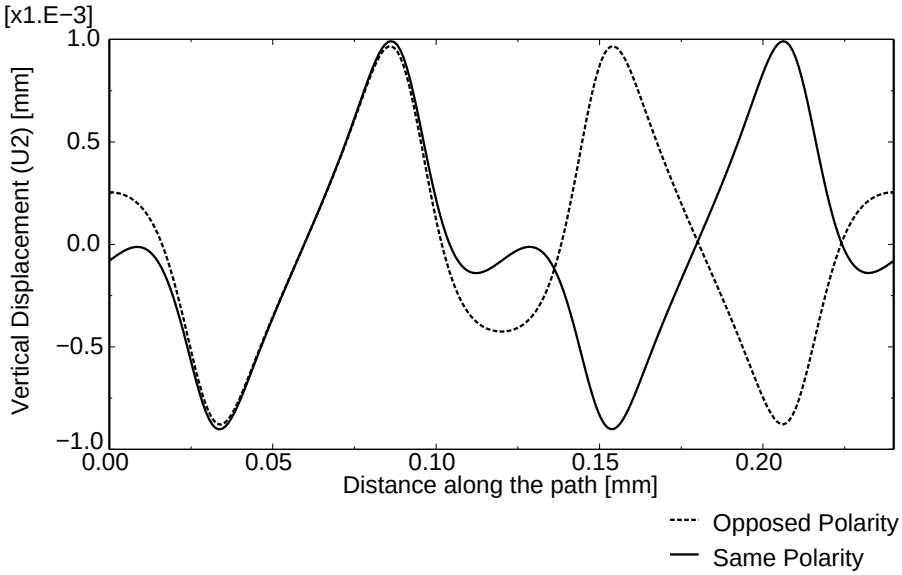

Figure 5: Vertical displacement of the top surface of the base film

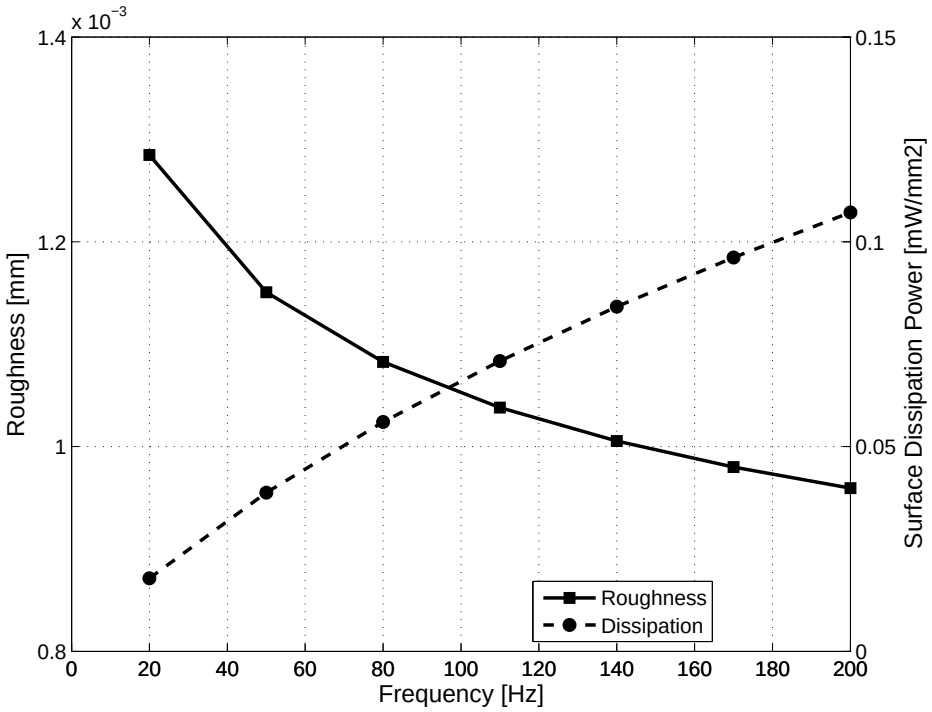

Figure 6: Roughness and Surface Dissipation Power as a function of the excitation frequency

Model	Vol. Frac.	RVE Width	Act. Width	Act. Thick.	Act. Offset	Frequency	Traction	E Actuator	E Top Film	Elements	Surf. Dis. Pwr.	Roughness
	[ ]	[mm]	[mm]	[mm]	[mm]	[Hz]	[MPa]	[GPa]	[GPa]	[ ]	[mW/mm^2]	[mm]
2D-P-01	0.1308	0.12	0.0600	0.0100	0.000	200	10	3	70	8040	0.1072	0.000959
2D-P-02	0.1308	0.12	0.0600	0.0100	0.000	170	10	3	70	8040	0.0961	0.000980
2D-P-03	0.1308	0.12	0.0600	0.0100	0.000	140	10	3	70	8040	0.0842	0.001005
2D-P-04	0.1308	0.12	0.0600	0.0100	0.000	110	10	3	70	8040	0.0709	0.001038
2D-P-05	0.1308	0.12	0.0600	0.0100	0.000	80	10	3	70	8040	0.0560	0.001083
2D-P-06	0.1308	0.12	0.0600	0.0100	0.000	50	10	3	70	8040	0.0388	0.001151
2D-P-07	0.1308	0.12	0.0600	0.0100	0.000	20	10	3	70	8040	0.0179	0.001285
2D-P-08	0.1308	0.12	0.0600	0.0100	-0.005	200	10	3	70	8809	0.0268	0.000327
2D-P-09	0.1308	0.12	0.0600	0.0100	0.005	200	10	3	70	8426	0.1935	0.001904
2D-P-10	0.1744	0.09	0.0600	0.0100	0.000	200	10	3	70	4428	0.1647	0.001084
2D-P-11	0.1046	0.15	0.0600	0.0100	0.000	200	10	3	70	5292	0.0829	0.000940
2D-P-12	0.0523	0.30	0.0600	0.0100	0.000	200	10	3	70	13621	0.0421	0.000944
2D-P-13	0.1308	0.12	0.0600	0.0100	0.000	200	10	3	70	1931	0.0951	0.000917
2D-P-14	0.1308	0.12	0.0600	0.0100	0.000	200	10	3	70	17394	0.1072	0.000959
2D-P-15	0.1308	0.12	0.0600	0.0100	0.000	200	10	3	70	4915	0.1052	0.000958
2D-P-16	0.0824	0.12	0.0238	0.0159	0.000	200	10	3	70	4101	0.0238	0.015874
2D-P-17	0.1602	0.12	0.0900	0.0082	0.000	200	10	3	70	4239	0.0274	0.000622
2D-P-18	0.1308	0.12	0.0600	0.0100	0.000	200	10	3	70	8830	0.1059	0.000956
2D-P-19	0.1308	0.12	0.0600	0.0100	0.000	200	10	3	70	8830 [1]	0.1078	0.000962
2D-P-20	0.1308	0.12	0.0600	0.0100	0.000	200	5	3	70	8830	0.0089	0.000377
2D-P-21	0.1308	0.12	0.0600	0.0100	0.000	200	15	3	70	8830	0.3405	0.001704
2D-P-22	0.1308	0.12	0.0600	0.0100	0.000	200	10	2	70	8830	0.1084	0.000968
2D-P-23	0.1308	0.12	0.0600	0.0100	0.000	200	10	1	70	8830	0.1168	0.000990
2D-P-24	0.1308	0.12	0.0600	0.0100	0.000	200	10	3	50	8830	0.1061	0.000954
2D-P-25	0.1308	0.12	0.0600	0.0100	0.000	200	10	3	30	8830	0.1065	0.000950
2D-P-26	0.1308	0.12	0.0600	0.0100	0.000	200	10	3	30	9070 [2]	0.1065	0.000950

Table 4: Results of the parametric study.

[a] This model has been solved using quadratic elements (`CPE8R` and `CPE8RH`).
[b] Two elements were used through the thickness of the top film in this model.

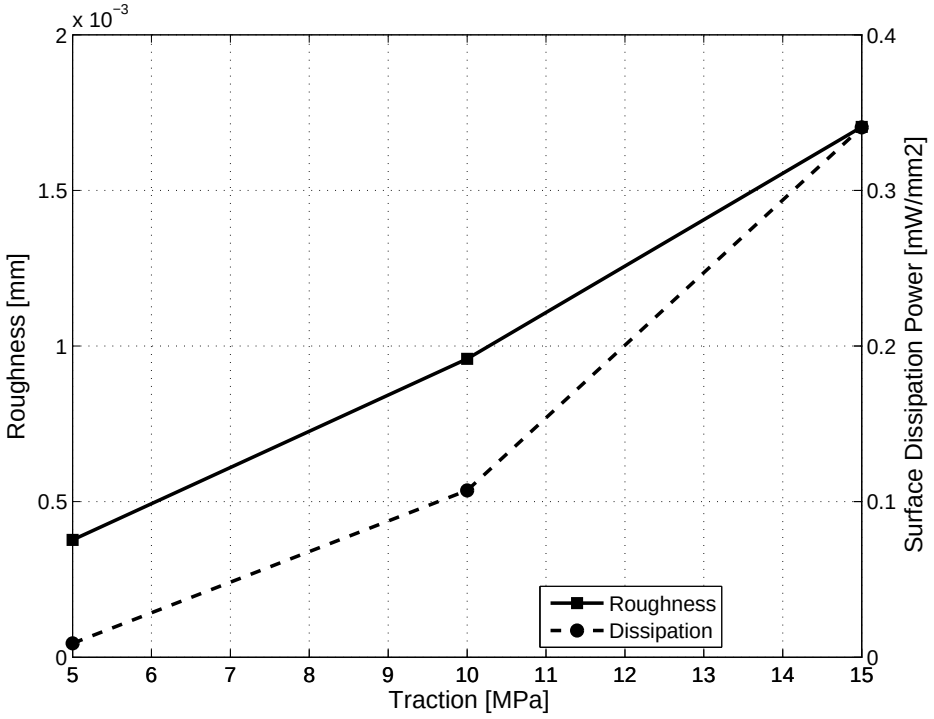

Figure 7: Roughness and Surface Dissipation Power as a function of the surface traction magnitude

same magnitude but opposite directions in the top and bottom surfaces of the actuators. Here, the magnitude of the traction, and thus torque, will be varied to study the response of the APF.

Roughness and Surface Dissipation Power as a function of the surface traction magnitude are shown in Figure 7. The models used to create these figures are 2D-P-01, 2D-P-20 and 2D-P-21, which are listed in Table 4. As it can be seen in Figure 7, the response is non-linear, as it was expected because the base film material is not linear. Both roughness and the surface dissipation power are higher when the applied torque was increased (see Figure 7). Note that in order to increase the roughness by a 78 %, the dissipation increases 300 %. This fact puts in evidence the non-linear behavior of the viscous effects.

To study the effect of the volume fraction V_f, the width of the RVE is changed and the response is analyzed. The results from models 2D-P-01 and 2D-P-10 to 2D-P-12 are plotted in Figure 8. The roughness is unchanged because it is measured locally as the peak to peak displacement of the surface above any actuator. The power dissipation increases with volume fraction.

The actuator and top film Young's modulus are varied to study the impact on the response. In the models 2D-P-22 and 2D-P-23, the actuator's modulus is set to 2000 MPa and 1000 MPa, respectively, while keeping all the other parameters equal to the ones of the reference model 2D-P-01. The top film modulus is reduced from 70 000 MPa to 50 000 MPa and 30 000 MPa in the models 2D-P-24 and 2D-P-25, respectively. For the two latter models, all the other parameters are the same as in model 2D-P-01.

The surface dissipation power and roughness results for all the aforementioned models are included in Table 4. As it can be seen from the results, the impact on the roughness and dissipation power are very small even for changes in the order of 300 % in the actuator Young's modulus and 233 % in the top film Young's modulus. The most noticeable change is in the surface dissipation power, when the actuators Young's modulus is reduced to 1000 MPa. The change in the response

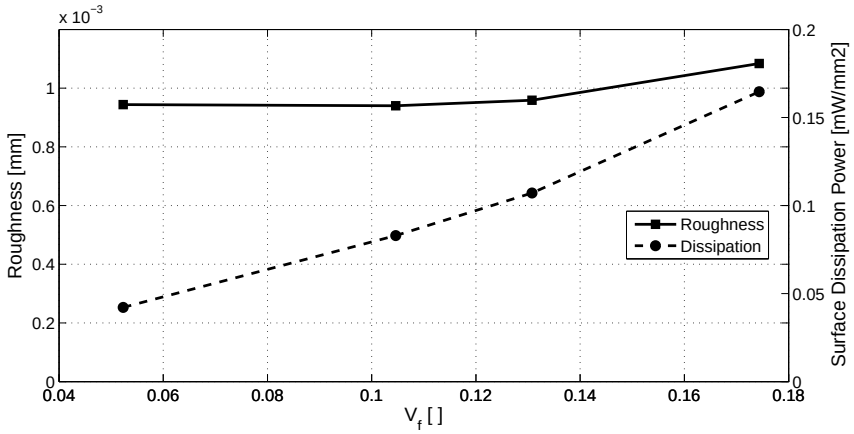

Figure 8: Roughness and Surface Dissipation Power as a function of V_f for the 2D model

due to changes in the top film modulus are negligible. This latter fact happens because the top film, although it has a higher modulus than the base film, it is 1000 times thinner; and the bending stiffness of a plate is proportional to its thickness cubed.

A convergence study is performed to evaluate the discretization used. In the h-refinement method, the same type of elements is used, but the size of the elements is changed [32]. For this case, complete regeneration is used. From a computational point of view this is very expensive, but feasible. Meshes with different element sizes are generated and the results are compared. If the problem is mesh independent, the results should converge asymptotically as the element size is reduced. From the results of models 2D-P-01, 2D-P-13, 2D-P-14 and 2D-P-15, displayed in Figure 9, it can be seen that the results are very similar when the number of elements is increased from 8040 to 17394, showing that the solution is convergent.

In the p-refinement method, the original mesh is kept, but the degree of the elements is changed. ABAQUS® has to types of elements available, linear and quadratic. In order to compare the results, two models are analyzed; one with linear (4 noded), plane strain continuum elements and the other with quadratic (8 noded) elements. The ratio between the roughness and surface dissipation power between both meshes are 1.0063 and 1.0176, respectively. The results for these models are listed in Table 4 as 2D-P-18 and 2D-P-19, with the latter one meshed with quadratic elements.

From the mesh dependency analysis, it can be concluded that for a two-dimensional model with an RVE width of 120 µm and thickness of 30.03 µm, the change in the results is marginal for meshes with more than 4900 elements. Also, the use of quadratic elements showed a very small variation in the results.

9 Parameter Characterization for the Bergström-Boyce Model

The parameters of the BB model can be fit to uniaxial experimental data using the methodology described in this section. Then, the material model is exercised by fitting available uniaxial stress-strain data for nitrile rubber [33]. The procedure assumes that the material is incompressible. A minimization algorithm, such as `FMINSEARCHCON.m` [34], is used to find the values of the parameters that correlate the material model to the data.

The experimental data needed to do the uniaxial fit for the BB model is composed of time, true strain, and true stress. Since most of the experimental data available in the literature is in the form of nominal stress and strain, it must be converted to true values using

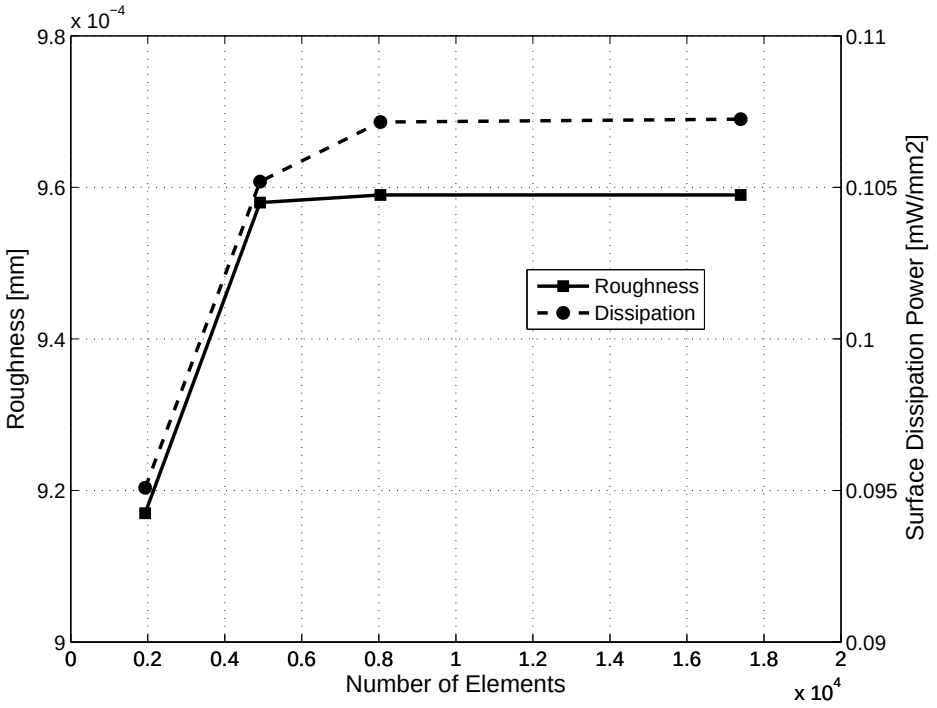

Figure 9: Roughness and Surface Dissipation Power as a function of the number of elements

$$\epsilon = \ln(\lambda) = \ln(1 + \epsilon^{\text{eng}}) \tag{4}$$

$$\sigma = \sigma^{\text{eng}}\lambda \tag{5}$$

In this work, the true stress σ is considered to be a function of both time t and true strain ϵ history. Therefore, $\sigma = \sigma(t, \epsilon(t))$.

The BB model has the ability to capture the rate dependent behavior of elastomers. But in order to do a successful fit of the parameters that define this model, it is imperative that the experimental data is sampled, at least, for two different strain rates. Therefore, the computer implementation of the algorithm must allow input of multiple sets of experimental data.

Since experimental data is available from uniaxial tests only, in this work, the constitutive equation of the BB material model is reduced to the uniaxial loading case. The BB model consists of two networks, A and B, in parallel. Network A is hyperelastic, and network B is both hyperelastic and time-dependent (viscous).

The stress $\sigma_{A_{11}}$ in network A is expressed in terms of the stretch in the loading direction by

$$\sigma_{A_{11}} = \frac{\mu_A}{\overline{\lambda^*}} \frac{\mathcal{L}^{-1}\left(\overline{\lambda^*}/\lambda_A^{\text{lock}}\right)}{\mathcal{L}^{-1}\left(1/\lambda_A^{\text{lock}}\right)} \left(\lambda^2 - \frac{1}{\lambda}\right) \tag{6}$$

where $\mu_A, \lambda_A^{\text{lock}}$ are the hyperelastic parameters of network A (initial shear modulus and limiting chain stretch, respectively). $\mathcal{L}^{-1}(x)$ is the inverse Langevin function and $\overline{\lambda^*}$ is the effective distortional chain stretch given by

$$\overline{\lambda^*} = \sqrt{\frac{1}{3}\left(\lambda^2 + \frac{2}{\lambda}\right)} \tag{7}$$

The stress component $\sigma_{B_{11}}$ in network B is given by

$$\sigma_{B_{11}} = \frac{\mu_B}{\overline{\lambda_B^{e*}}} \frac{\mathcal{L}^{-1}\left(\overline{\lambda_B^{e*}}/\lambda_B^{\text{lock}}\right)}{\mathcal{L}^{-1}\left(1/\lambda_B^{\text{lock}}\right)} \left(\lambda_B^{e^2} - \frac{1}{\lambda_B^e}\right) \tag{8}$$

where μ_B and λ_B^{lock} are the parameters of the hyperelastic part of network B. It is common to express μ_B as a function of μ_A, introducing the parameter s

$$\mu_B = \mu_A s \tag{9}$$

and usually, it is assumed that the limiting chain stretch λ^{lock} is the same for both networks,

$$\lambda^{\text{lock}} = \lambda_A^{\text{lock}} = \lambda_B^{\text{lock}} \tag{10}$$

The effective distortional chain stretch in the elastic part of network B is given by

$$\overline{\lambda_B^{e*}} = \sqrt{\frac{1}{3}\left((\lambda_B^{e*})^2 + \frac{2}{\lambda_B^{e*}}\right)} \tag{11}$$

For the uniaxial loading and incompressible material the flow rule is given by,

$$\dot{\lambda}_B^p = \left(\frac{\dot{\gamma}_0}{\tau_{\text{base}}^m}\right) \left(\sqrt{\frac{1}{3}\left((\lambda_B^p)^2 + \frac{2}{\lambda_B^p}\right)} - 1 + E\right)^c \left(\sqrt{\frac{2}{3}}\,|\sigma_{B_{11}}|\right)^m \left[\sqrt{\frac{2}{3}}\text{sign}(\sigma_{B_{11}})\right] \lambda_B^p \tag{12}$$

where $\dot{\gamma}_0/\tau_{\text{base}}^m, c$ and m are material parameters, E is a constant added to improve the numerical convergence. Equation (12) is a first-order ordinary differential equation (ODE) in λ_B^p. Therefore, only one initial condition is needed to solve the ODE.

Given a strain-time curve, the constitutive equations (6, 8) will calculate the stress. The resulting ODE (12) is solved numerically using MATLAB®'s built-in `ode23` solver. At the beginning of each experimental data set, the strain and stress are known and equal to zero. Therefore, the total stretch is equal to the elastic and viscous stretches, $\lambda = \lambda_B^e = \lambda_B^p = 1$. This becomes the initial condition for the ODE solver for the first time step of every experimental data set. The ODE solver integrates the flow rule (12) from the current time step to the following. Once it solves for viscous stretch λ_B^p for the following time step, the elastic stretch λ_B^e is calculated using the following product decomposition

$$\mathbf{F}_B = \mathbf{F}_B^e \cdot \mathbf{F}_B^p \tag{13}$$

for the uniaxial case ($\lambda = \lambda_B^e \lambda_B^p$).

Having the elastic stretch λ_B^e for network B and the total stretch λ, it is possible to find the stress in both networks, A and B. At this point, all the ingredients required to start the next iteration are available. The viscous stretch λ_B^p calculated at this step will become the initial condition to solve the ODE for the following step.

The error function uses the constitutive equations for the uniaxial loading case of the incompressible BB model (6, 8 and 12) and calculates the difference between the stress calculated by the constitutive equation and the experimental stress. The smaller the difference, the better the fit is.

There are different functions that can be used to measure the error. In this work, the Normalized Median Absolute Difference is used

$$\text{ERROR} = 100 \frac{\sum_{i=1}^{n} \left| \sigma_i^{\text{exp}} - \sigma_i^{\text{fit}} \right|}{\sum_{i=1}^{n} |\sigma_i^{\text{exp}}|} \tag{14}$$

where n is the number of experimental data points, σ^{exp} is vector containing all the measured stresses and σ^{fit} is the vector containing the stresses calculated using the constitutive law and the current value of the parameters. The minimization process is driven by reducing the error given by (14).

The program is demonstrated by fitting available uniaxial experimental data from Reference [33] for nitrile rubber (NR), assumed to be incompressible, i.e., $s = 2.3$, $\dot{\gamma}_0/\tau_{\text{base}}^m = 0.54/(sMPa)$, $m = 4.5$, and $c = -0.99$.

10 Future Work

The development of the process to apply the conductive coating to the surface of the PDLC film has not been completed yet. Once this is done, a non-contact perfilometer can be used to measure the roughness of the surface when the electric field is applied and held constant. Another option is to place the un-coated PDLC film between two panes of indium tin oxide (ITO) coated glass, so that the potential differential can be applied between the glasses and the depth of the valleys measured using optical interferometry. This APF would lack of the conductive thin film, which modifies the mechanical behavior of the film, and the top glass prevents peaks from appearing–only valleys can appear below the rigid top glass. Furthermore, the APF would be different from the intended for the applications, where the conductive coating is required. As it can be seen, since some processing steps are still under development, we have focused on computational modeling that can help us better define the materials, dimensions, and other system parameters in support of future experimentation.

11 Conclusions

Sophisticated three-dimensional models like the ones presented in Section 6 give the most accurate and precise results, while simplified two-dimensional models, like the ones presented in Section 8, allow one to run many cases (about twenty-five in this manuscript) in an affordable amount of time. The ratio between the results of three-dimensional and a two-dimensional models can be used as a design tool, to extrapolate the results of the simplified two-dimensional models to the three-dimensional case, as a function of the volume fraction. A remarkable fact from the results of the three-dimensional models is that as the volume fraction V_f decreases, both the total dissipation power and the roughness reach limit values. A similar behavior can be observed for the roughness and surface dissipation ratios analyzed in Section 7. Large changes in the top film and actuator modulus did not show a significant impact in the results. Therefore, it could be said that the response of the APF has a very small sensitivity to these parameters. In conclusion, a varied set of powerful tools for the design and analysis of actuated polymer films were introduced in this work. It is expected that these procedures will be valuable for material selection, application development, and to design experiments that can be used to measure some of the results that are numerically predicted in this study.

Acknowledgements

The authors wish to thank Dr. Wade Huebsch for his insight into potential application of actuated polymer films for aerodynamic flow control. The financial support provided by NASA EPSCoR grant NNH09ZNE002C is appreciated.

A PYTHON Script

In order to calculate the dissipated energy correctly, a PYTHON script was developed. This script is ran after the analysis is done and it uses the output database from ABAQUS® . The field outputs that this script must read are:

LE Logarithmic Strain Tensor

S Cauchy Stress Tensor

IVOL Integration Point Volume

The script must be able also to query the history output `ALLSE`, the total recoverable (elastic) strain energy at the last frame (time step) of the analysis.

The total strain energy can be calculated using numerical integration as

$$\mathcal{W} = \sum_{k=2}^{n} \sum_{l=1}^{m} \sum_{i=1}^{p} \left(\mathrm{LE}_i^{k,l} - \mathrm{LE}_i^{k-1,l} \right) \frac{\left(\mathrm{S}_i^{k,l} + \mathrm{S}_i^{k-1,l} \right)}{2} \frac{\left(\mathrm{IVOL}^{k,l} + \mathrm{IVOL}^{k-1,l} \right)}{2} \tag{15}$$

where n is the number of frames in the analysis (time steps), m is the number of integration points in the model and p is the number of independent components of the stress and strain tensors in the analysis. For example, in a three-dimensional analysis $p = 6$, while in a plane strain analysis $p = 3$. The first (outer) summation loops over the frames of the analysis, the second over integration points and the third over the components of the stress and strain tensors.

To save computational time, the integration can be carried out only in the regions made of hysteretic material. For an elastic material, the strain energy is equal to zero when the material is unloaded. Viscous materials exhibit a phenomena where the strains lag behind the stresses. This means that even when the stress is removed, the strain might not be equal to zero. Therefore, the script must subtract the recoverable elastic strain energy from the total strain energy in order to calculate the dissipated energy.

$$\mathcal{U}_{\text{creep}} = \mathcal{W} - \texttt{ALLSE}|_{k=n} \tag{16}$$

where $\mathcal{W}$ is given by (15) and $\texttt{ALLSE}|_{k=n}$ is the value of the recoverable strain energy at the last frame for the region where $\mathcal{W}$ was calculated.

A temporary variable is created to hold the frame repository. This noticeably speeds up the process. Further performance improvements could be done by accessing the output database using C++ instead of PYTHON.

References

[1] J. Doane, A. Golemme, J. West, J. Whitehead Jr, B. Wu, Polymer dispersed liquid crystals for display application, Molecular Crystals and Liquid Crystals 165 (1) (1988) 511–532.

[2] P. S. Drzaic, Nematic droplet/polymer films for high-contrast coloured reflective displays, Displays 12 (1) (1991) 2 – 13. doi:DOI:10.1016/0141-9382(91)90022-6.
URL http://www.sciencedirect.com/science/article/pii/0141938291900226

[3] K. Tanaka, K. Kato, S. Tsuru, S. Sakai, Holographically formed liquid-crystal/polymer device for reflective color display, Journal of the Society for Information Display 2 (1994) 37.

[4] M. Mucha, Polymer as an important component of blends and composites with liquid crystals, Progress in polymer science 28 (5b) (2003) 837–873.

[5] G. Crawford, R. Polak, A. Scharkowski, L. Chien, J. Doane, S. Zumer, Nematic director-fields captured in polymer networks confined to spherical droplets, Journal of applied physics 75 (4) (1994) 1968–1971.

[6] T. J. Bunning, L. V. Natarajan, V. P. Tondiglia, R. L. Sutherl, Holographic polymer-dispersed liquid crystals (h-pdlcs)., Annual Review of Materials Science 30 (1) (2000) 83.

[7] Y. J. Jeon, Y. Bingzhu, J. T. Rhee, D. L. Cheung, M. Jamil, Application and new developments in polymer-dispersed liquid crystal simulation studies, Macromolecular Theory and Simulations 16 (7) (2007) 643–659. doi:10.1002/mats.200700008.
URL http://dx.doi.org/10.1002/mats.200700008

[8] R. Pogue, R. Sutherland, M. Schmitt, L. Natarajan, S. Siwecki, V. Tondiglia, T. Bunning, Electrically switchable bragg gratings from liquid crystal/polymer composites, Applied spectroscopy 54 (1) (2000) 12–28.

[9] A. Fuh, M. Tsai, L. Huang, T. Liu, Optically switchable gratings based on polymer-dispersed liquid crystal films doped with a guest–host dye, Applied physics letters 74 (18) (1999) 2572–2574.

[10] N. J. Morris, J. M. Gutierrez, E. J. Barbero, D. R. Cairns, Polymer skins with switchable roughness, in: ASME Conference on Smart Materials, Adaptive Structures and Intelligent Systems, Phoenix, Arizona, USA, 2011.

[11] W. W. Huebsch, Two-dimensional simulation of dynamic surface roughness for aerodynamic flow control, AIAA Journal of Aircraft 43(2) (2006) 353–362.

[12] B. Matheis, W. Huebsch, A. Rothmayer, Separation and unsteady vortex shedding from leading edge surface roughness, Tech. rep., Iowa State University (2004).

[13] Huebsch, W.W., Gall, P.D., Hamburg, S.D. and Rothmayer, A.P., Dynamic Roughness as a Means of Leading Edge Separation Flow Control", AIAA Journal of Aircraft, accepted.

[14] D. R. Cairns, M. S. Shafran, K. A. Sierros, W. W. Huebsch, A. J. Kessman, Stimulus-responsive fluidic dispersions of rod shaped liquid crystal polymer colloids, Materials Letters 64 (10) (2010) 1133 – 1136.

[15] M. S. Shafran, Responsive liquid crystal polymer rods, Master's thesis, College of Engineering and Mineral Resources at West Virginia University (2008).

[16] E. M. Arruda, M. C. Boyce, A three-dimensional constitutive model for the large stretch behavior of rubber elastic materials, Journal of the Mechanics and Physics of Solids 41 (2) (1993) 389 – 412.

[17] E. Barbero, R. Luciano, Micromechanical formulas for the relaxation tensor of linear viscoelastic composites with transversely isotropic fibers, International Journal of Solids and Structures 32 (13) (1995) 1859–1872.

[18] J. S. Bergström, Large strain time-dependent behavior of elastomeric materials, Ph.D. thesis, MIT (1999).

[19] J. S. Bergström, M. C. Boyce, Constitutive modeling of the large strain time-dependent behavior of elastomers, Journal of the Mechanics and Physics of Solids 46 (5) (1998) 931–954.

[20] J. S. Bergström, M. C. Boyce, Constitutive modeling of the time-dependent and cyclic loading of elastomers and application to soft biological tissues, Mechanics of Materials 33 (9) (2001) 523–530.

[21] J. S. Bergström, M. C. Boyce, Mechanical behavior of particle filled elastomers, Rubber Chemistry and Technology 72 (4) (1999) 633–656.

[22] J. S. Bergström, M. C. Boyce, Large strain time-dependent behavior of filled elastomers, Mechanics of Materials 32 (11) (2000) 627–644.

[23] H. Dal, Computational aspects of Bergstrom-Boyce finite viscoelasticity model, in: C. models for rubber (Ed.), Constitutive models for rubber, Vol. 5, Balkema, 2008.

[24] P. Areias, K. Matous, Finite element formulation for modeling nonlinear viscoelastic elastomers, Computer Methods in Applied Mechanics and Engineering 197 (51-52) (2008) 4702 – 4717.

[25] H. Dal, M. Kaliske, Bergstrom-Boyce model for nonlinear finite rubber viscoelasticity: theoretical aspects and algorithmic treatment for the FE method, Computational Mechanics 44 (6) (2009) 809–823.

[26] E. J. Barbero, Creep and Fatigue in Polymer Matrix Composites, Woodhead Publishing, 2010, Ch. Time-temperature-age superposition principle for predicting long-term response of linear viscoelastic materials, pp. 48–69.

[27] E. J. Barbero, Introduction to Composite Materials Design–Second Edition., CRC Press, 2010. URL http://www.mae.wvu.edu/barbero/icmd/

[28] Computer aided material preselection by uniform standards, http://www.campusplastics.com/ (2009).

[29] E. J. Barbero, Finite Element Analysis of Composite Materials, CRC Press, 2007. URL http://www.mae.wvu.edu/barbero/feacm/

[30] D. R. Cairns, M. Sibulki, G. P. Crawforda, Switching dynamics of suspended mesogenic polymer microspheres, Applied Physics Letters 78 (18) (2001) 2643–2645.

[31] Dassault Systèmes, ABAQUS Theory Manual (6.9) (2010).

[32] O. Zienkiewicz, R. Taylor, J. Zhu, The finite element method: its basis and fundamentals, The Finite Element Method, Elsevier Butterworth-Heinemann, 2005.

[33] J. S. Bergström, http://polymerfem.com. [link].
URL http://polymerfem.com

[34] J. D'Errico,
http://www.mathworks.com/matlabcentral/fileexchange/13469-fminsearchcon (December 2006).